Experimental determination of the Hamiltonian for synchrotron motion with rf phase modulation

H. Huang,[1] M. Ball,[1] B. Brabson,[1] J. Budnick,[1] D. D. Caussyn,[1] A. W. Chao,[2] J. Collins,[1] V. Derenchuk,[1] S. Dutt,[2] G. East,[1] M. Ellison,[1] D. Friesel,[1] B. Hamilton,[1] W. P. Jones,[1] S. Y. Lee,[1] D. Li,[1] M. G. Minty,[3] S. Nagaitsev,[1] K. Y. Ng,[4] X. Pei,[5] A. Riabko,[1] T. Sloan,[1] M. Syphers,[2] L. Teng,[6] Y. Wang,[1] Y. T. Yan,[2] and P. L. Zhang[2]

[1]*Indiana University Cyclotron Facility, Indiana University, Bloomington, Indiana 47405*
[2]*The Superconducting Super Collider Laboratory, 2550 Beckleymeade Avenue, Dallas, Texas 75237-3946*
[3]*Stanford Linear Accelerator Center, MS26, Box 4349, Stanford, California 94309*
[4]*Fermilab, P.O. Box 500, Batavia, Illinois 60510*
[5]*Brookhaven National Laboratory, Upton, New York 11973*
[6]*Argonne National Laboratory, 9700 South Cass Avenue, Argonne, Illinois 60439*

(Received 28 June 1993)

Synchrotron motion with rf phase modulation was studied experimentally. Poincaré maps in the resonant precessing frame were obtained from the experimental data and compared with the tori of the resonant Hamiltonian. Our experimental data revealed island structure in longitudinal phase space. Experimental results for synchrotron motion excited by phase modulation at the third harmonic of the synchrotron frequency are also reported.

PACS number(s): 41.85.−p, 03.20.+i, 05.45.+b, 29.20.Dh

I. INTRODUCTION

Synchrotron motion occurs in two dimensions of the six-dimensional phase space for particle motion in a circular accelerator. Therefore, longitudinal beam dynamics studies associated with the synchrotron motion can be as important as the transverse dynamics associated with the betatron motion. An actual accelerator may contain longitudinal or transverse error fields, which vary with time randomly or sinusoidally and cause unpredictable outcomes resulting in degrading the performance of colliders or storage rings. Indeed, emittance blowup and beam loss due to rf noise have been observed in the Super Proton Synchrotron at CERN [1]. Understanding the effects of these time-varying devices on beam dynamics is important in setting tolerance levels during machine design, construction, and commissioning. The studies of longitudinal beam dynamics may also lead to a better control of the time-varying components for emittance dilution, super slow beam extraction, controlled phase space manipulations, etc. [1]. Because of these possible benefits to future accelerators, careful experimental and theoretical studies of synchrotron motion with rf phase modulation are needed.

The equation of motion for transverse oscillations of a particle trapped in a one degree of freedom resonance island, in the presence of betatron tune modulation, is equivalent to that of synchrotron motion with phase modulation. Studies of synchrotron motion with rf phase modulation have added importance for understanding the consequences of transverse betatron tune modulation.

The rf phase modulation may arise from rf noise, rf power supply ripple, a driven rf phase shifter, or synchro-betatron coupling. The synchro-betatron resonance may be excited by a finite chromaticity, dispersion function in rf cavities, transverse wake fields, a beam-beam interaction, and a time-varying transverse dipole field located at a nonzero dispersion region. In the latter case, the path length that the particle traverses in one revolution is modulated by $\Delta C = \sum_i D_i \theta_i(t)$, where $\theta_i(t)$ is the modulation dipole kick angle and D_i is the dispersion function at the dipole location [2]. Therefore the arrival time of the particle at the rf gap relative to the rf wave will be modulated. The result is equivalent to that of rf phase modulation on synchrotron motion [3]. Recently, experimental measurements of the beam response due to the rf phase modulation have been reported [4]. Although our preliminary data analysis was shown to agree well with single particle tracking calculations, data analysis based on a Hamiltonian formulation was missing. This work is intended to bridge the gap between the report of the measured data and our understanding of particle motion based on the framework of the Hamiltonian dynamics.

The plan of the paper is as follows. In Sec. II, we discuss the properties of the Hamiltonian for the synchrotron motion with phase modulation. The longitudinal phase space will be transformed to action-angle coordinates, where the Hamiltonian in the resonant rotating frame will be derived. In Sec. III, the experimental procedure and the data analysis using Hamiltonian dynamics will be reported. The conclusions are given in Sec. IV.

II. HAMILTONIAN OF SYNCHROTRON MOTION WITH PHASE MODULATION

The synchrotron mapping equations for a single particle, with rf phase modulation, are given by [5]

 ©1993 The American Physical Society

$$\phi_{n+1} = \phi_n + 2\pi h\eta \left(\frac{\Delta p}{p}\right)_n + (\varphi_{n+1} - \varphi_n),$$
$$\left(\frac{\Delta p}{p}\right)_{n+1} = \left(\frac{\Delta p}{p}\right)_n + \frac{eV}{\beta^2 E}\sin\phi_{n+1} - \lambda\left(\frac{\Delta p}{p}\right)_n, \tag{2.1}$$

where $(\frac{\Delta p}{p})$ and ϕ are conjugate phase-space coordinates of the synchrotron motion describing the fractional momentum deviation and the synchrotron phase, respectively, h is the harmonic number, η is the phase slip factor, $\varphi_n = a\sin\nu_m\theta_n$ is the sinusoidal phase modulation function, θ_n is the cumulative orbital angle at the nth revolution used for the time variable, ν_m is the modulation tune or the ratio of the modulation frequency to the revolution frequency, a is the phase error modulation amplitude, V is the effective rf voltage, βc and E are, respectively, the speed and energy of an orbiting particle, and λ is the phase-space damping parameter related to electron cooling at the IUCF Cooler Ring, or synchrotron radiation damping in electron storage rings.

Defining the normalized momentum δ as $\frac{h\eta}{\nu_s}(\frac{\Delta p}{p})$, where $\nu_s = \sqrt{\frac{h|\eta|eV}{2\pi\beta^2 E}}$ is the synchrotron tune, the difference equations, Eq. (2.1), can be written as

$$\phi_{n+1} = \phi_n + 2\pi\nu_s\delta_n + 2\pi\nu_m a\cos\nu_m\theta_n\ ,$$
$$\delta_{n+1} = \delta_n - 2\pi\nu_s\sin\phi_{n+1} - 2\pi\frac{2\alpha}{\omega_0}\delta_n, \tag{2.2}$$

where ω_0 is the angular revolution frequency, $\alpha = \frac{\omega_0}{4\pi}\lambda$, and the derivative of the phase-modulation function, $\nu_m a\cos\nu_m\theta_n$, is used for $(\varphi_{n+1} - \varphi_n)/2\pi$ in Eq. (2.2). Without external rf phase-modulation, the synchrotron phase equation becomes

$$\frac{d^2\phi}{dt^2} + 2\alpha\frac{d\phi}{dt} + \omega_s^2\sin\phi = 0,$$

where $\omega_s = \omega_0\nu_s$ is the angular synchrotron frequency. The exponential-folding time of the phase-space damping is $\frac{1}{\alpha}$. The damping parameter for the IUCF Cooler Ring can be obtained from the damping of the phase amplitude of the coherent synchrotron oscillation following a phase kick. Figure 1 shows the measured phase of the bunch as a function of the turn number after a phase kick. Measuring the damping rates after phase kicks, the damping parameter α was found to be limited about $\alpha \approx 3.0 \pm 1.0$ s^{-1} during this experiment, which was much smaller than the synchrotron angular frequency $\omega_s = 3342\ s^{-1}$. Therefore the electron cooling is not very important to our data analysis for the transient solutions of Eq. (2.2). Neglecting the damping term by setting $\alpha = 0$, Eq. (2.2) can be derived from the following Hamiltonian:

$$H = \frac{1}{2}\nu_s\delta^2 + \nu_s[1 - \cos\phi] + \nu_m a\delta\cos\nu_m\theta, \tag{2.3}$$

where the perturbing potential created by the rf phase modulation depends linearly on the momentum. To remove momentum dependence, we make a canonical transformation using the following generating function:

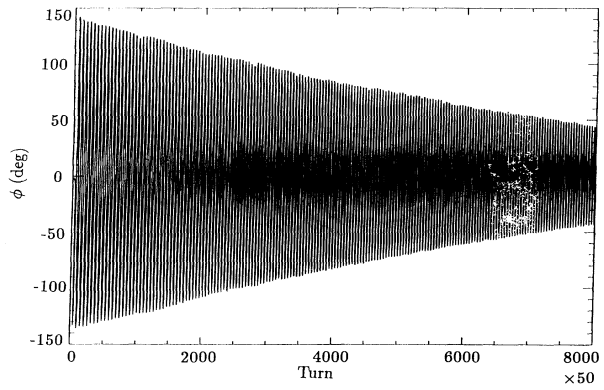

FIG. 1. The measured phase oscillation following a phase kick. The damping coefficient, obtained from the exponential-folding time of the phase amplitude, is about 0.34 s.

$$F_2(\phi, \tilde{\delta}) = (\phi - a\sin\nu_m\theta)\tilde{\delta} \tag{2.4}$$

to obtain the coordinate transformation $\delta = \tilde{\delta}$, $\tilde{\phi} = \phi - a\sin\nu_m\theta$. The conjugate phase coordinate $\tilde{\phi}$ is the phase displacement measured relative to the reference frame at the fixed revolution frequency. The new Hamiltonian becomes

$$H = \frac{1}{2}\nu_s\tilde{\delta}^2 + \nu_s[1 - \cos(\tilde{\phi} + a\sin\nu_m\theta)]. \tag{2.5}$$

To study the resonant structure of Eq. (2.5), we transform the phase-space coordinates $(\tilde{\phi}, \tilde{\delta})$ into the action-angle variables (J, ψ), where the action of the Hamiltonian is given by

$$J = \frac{1}{2\pi}\oint\tilde{\delta}d\tilde{\phi}. \tag{2.6}$$

In the limit of small action, i.e., $J \leq 2$, the canonical transformation can be accomplished by using the generating function

$$F_1(\tilde{\phi}, \psi) = -\frac{\tilde{\phi}^2}{2}\tan\psi \tag{2.7}$$

to obtain $\tilde{\phi} = \sqrt{2J}\cos\psi$, $\tilde{\delta} = -\sqrt{2J}\sin\psi$. The new Hamiltonian becomes

$$H = \nu_s J\sin^2\psi + \nu_s[1 - \cos(\sqrt{2J}\cos\psi + a\sin\nu_m\theta)]$$
$$\approx \nu_s J - \frac{\nu_s}{16}J^2 + \Delta H_0 + \sum_{k=0}^{\infty}[\Delta H_{2k+1}^{(+)} + \Delta H_{2k+1}^{(-)}], \tag{2.8}$$

where

$$\Delta H_0 = \nu_s\left[-\frac{J}{2}\cos 2\psi - 2\sum_{k=1}^{\infty}(-1)^k J_{2k}(\sqrt{2J})\cos 2k\psi\right]$$

arises from the approximation of the canonical transformation by using Eq. (2.7) to obtain the action-angle variables. Here J_n's are the Bessel functions of order n. With a canonical transformation to the true action-angle variables, ΔH_0 will be independent of ψ, as shown in the Appendix. The unperturbed synchrotron tune is amplitude

dependent and is given approximately by $\tilde{\nu}_s \approx \nu_s(1-\frac{J}{8})$. This is a good approximation to the exact synchrotron tune, valid up to about $J \leq 2$.

The perturbed Hamiltonian arising from the external rf phase modulation is given by

$$\Delta H^{(\pm)}_{2k+1} = (-1)^k \nu_s a J_{2k+1}(\sqrt{2J}) \sin[\nu_m \theta \pm (2k+1)\psi], \quad k = 0, 1, \ldots . \quad (2.9)$$

Here the $\pm$ components of the perturbing potential depict, respectively, the oscillating components of the sinusoidal rf phase modulation in phase or out of phase with the synchrotron oscillations. The external modulation terms $\Delta H^{(-)}_{2k+1}$ become important when the modulation frequency is in resonance with a harmonic of the natural synchrotron frequency of the system, i.e., $\nu_m \approx (2k+1)\nu_s$. These resonances, created by the external harmonic phase modulation, are called parametric resonances [6].

A. Tori at the first order synchrotron resonance

When the modulation frequency is near one of the harmonics of the synchrotron frequency, the parametric resonance term in the Hamiltonian of Eq. (2.9) becomes important. Consider the resonance near the first harmonic. The coordinate system of the resonant precessing frame can be obtained using the generating function

$$F_2(\psi, \tilde{J}) = \left(\psi - \nu_m \theta - \frac{\pi}{2}\right) \tilde{J}, \quad (2.10)$$

where the coordinates are transformed according to $\tilde{\psi} = \psi - \nu_m\theta - \frac{\pi}{2}$, $J = \tilde{J}$. The corresponding new Hamiltonian becomes

$$\tilde{H} = (\nu_s - \nu_m)\tilde{J} - \frac{\nu_s}{16}\tilde{J}^2 - \frac{\nu_s a\sqrt{2\tilde{J}}}{2}\cos\tilde{\psi} + \Delta H(\tilde{J}, \tilde{\psi}, \theta). \quad (2.11)$$

The time dependent component of the perturbing Hamiltonian ΔH is a superposition of terms oscillating at frequencies of $2\nu_m, 4\nu_m, \ldots$, given by

$$\Delta H \approx \frac{\nu_s a\sqrt{2\tilde{J}}}{2}\cos(\tilde{\psi} + 2\nu_m\theta) + \frac{\nu_s \tilde{J}^2}{12}[\cos(2\tilde{\psi} + 2\nu_m\theta) - \tfrac{1}{4}\cos(4\tilde{\psi} + 4\nu_m\theta)] + \cdots, \quad (2.12)$$

where the second term arises from ΔH_0 discussed earlier.

In the resonant precessing frame, the time independent part of the Hamiltonian contributes coherently to perturbing kicks arising from the stationary phase (or resonance) condition $\frac{d\tilde{\psi}}{d\theta} \approx 0$. Particle motion is therefore strongly perturbed by the external modulation when $\nu_m \approx \nu_s$. Particle trajectories in phase space can be described by tori of the time averaged Hamiltonian

$$\langle H \rangle = (\nu_s - \nu_m)\tilde{J} - \frac{\nu_s}{16}\tilde{J}^2 - \frac{\nu_s a\sqrt{2\tilde{J}}}{2}\cos\tilde{\psi}, \quad (2.13)$$

which is an invariant. Hereafter, we drop the tilde notation for simplicity. A particle trajectory will follow a torus of the Hamiltonian flow. Figure 2 shows tori of Eq. (2.13) for various Hamiltonian values with $\nu_m = 0.935\nu_s$ and $a = 0.02$. The Hamilton's equations of motion are given by

$$\dot{J} = -\frac{1}{2}\nu_s a\sqrt{2J}\sin\psi,$$
$$\dot{\psi} = (\nu_s - \nu_m) - \frac{\nu_s}{8}J - \frac{\nu_s a}{2\sqrt{2J}}\cos\psi. \quad (2.14)$$

The fixed points of the Hamiltonian, which characterize the structure of resonant islands, are given by $\dot{J} = 0$, $\dot{\psi} = 0$. Using $g = \sqrt{2J}\cos\psi$, with $\psi = 0$ or π, to represent the phase coordinate of a fixed point, we obtain the equation for g as

$$g^3 - 16\left(1 - \frac{\nu_m}{\nu_s}\right)g + 8a = 0. \quad (2.15)$$

When the modulation tune is below the bifurcation tune ν_c, there are three solutions to Eq. (2.15), i.e. two stable fixed points (SFP's) and one unstable fixed point (UFP), given by

$$g_a(x) = -\frac{8}{\sqrt{3}}x^{1/2}\cos\frac{\xi}{3} \qquad (\psi = \pi),$$
$$g_b(x) = \frac{8}{\sqrt{3}}x^{1/2}\sin\left(\frac{\pi}{6} - \frac{\xi}{3}\right) \qquad (\psi = 0), \quad (2.16)$$
$$g_c(x) = \frac{8}{\sqrt{3}}x^{1/2}\sin\left(\frac{\pi}{6} + \frac{\xi}{3}\right) \qquad (\psi = 0),$$

where $x = 1 - \frac{\nu_m}{\nu_s}$, $x_c = 1 - \frac{\nu_c}{\nu_s}$, $\xi = \arctan\sqrt{(\frac{x}{x_c})^3 - 1}$, and ν_c, called the bifurcation tune, is given by

$$\nu_c = \nu_s[1 - \tfrac{3}{16}(4a)^{2/3}], \quad (2.17)$$

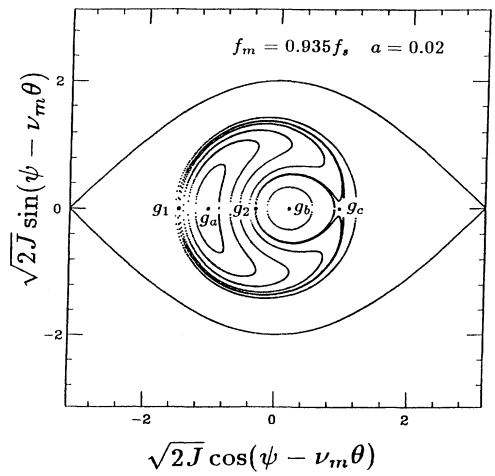

FIG. 2. The tori of the time averaged Hamiltonian at $\nu_m = 0.935\nu_s$ and $a = 0.02$. The separatrix for two resonant islands is the crescent shaped curve with cusps reaching the unstable fixed point.

or equivalently $x_c = \frac{3}{16}(4a)^{2/3}$. Here g_a and g_b are, respectively, the outer and the inner SFP's and g_c is the UFP. The reason that g_a and g_b are SFP's and g_c is the UFP will be discussed in Sec. II B. In the limit that $\nu_m \ll \nu_c$, we have $\xi \to \frac{\pi}{2}$, thus $g_a \to -4x^{1/2}$, $g_c \to 4x^{1/2}$, and $g_b \to 0$.

When the modulation frequency is approaching the bifurcation frequency from below, the UFP and the outer SFP's move in and the inner SFP moves out. At the bifurcation frequency, $x = x_c$ and $\xi = 0$, the UFP coincides with the inner SFP with $g_b = g_c = (4a)^{1/3}$.

Beyond the bifurcation frequency, $\nu_m > \nu_c$ $(x < x_c)$, there is only one real solution to Eq. (2.15) given by

$$g_a(x) = -(4a)^{1/3}\left\{ \left[\sqrt{1-\left(\frac{x}{x_c}\right)^3}+1\right]^{1/3} - \left[\sqrt{1-\left(\frac{x}{x_c}\right)^3}-1\right]^{1/3}\right\}. \quad (2.18)$$

In particular, when $x = 0$ $(\nu_m = \nu_s)$, we have $g_a = -(8a)^{1/3}$.

The particle motion in the phase space can be described by tori of constant Hamiltonian around SFP's. The phase amplitudes of the SFP's and UFP are marked on Fig. 2. The solutions g_a, g_b, and g_c of Eq. (2.15) are plotted in Fig. 3 as a function of the modulation frequency in $(\frac{x}{x_c})^{1/2}$ with $\nu_m \le \nu_s$. The torus that passes through the UFP is called the separatrix, which separates two stable islands. The intercepts of the separatrix with the phase axis, g_1 and g_2, are also shown in Figs. 2 and 3.

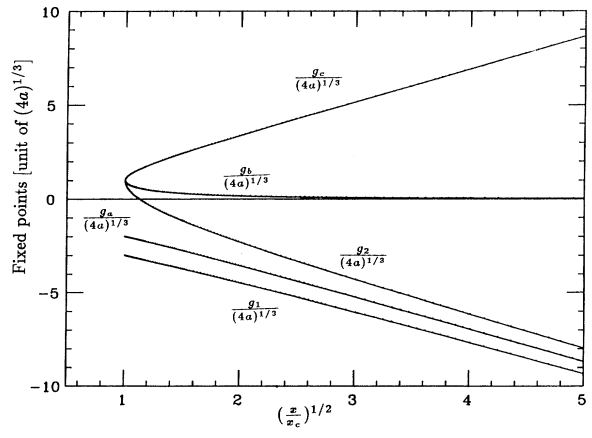

FIG. 3. The fixed points in unit of $(4a)^{1/3}$ are plotted as a function of the modulation frequency in $(\frac{x}{x_c})^{1/2}$, where $x = 1 - \frac{\nu_m}{\nu_s}$ and $x_c = \frac{3}{16}(4a)^{2/3}$ with a as the amplitude of the phase modulation. The SFP's are represented by $g_a/(4a)^{1/3}$ and $g_b/(4a)^{1/3}$ and the UFP is $g_c/(4a)^{1/3}$. The intercepts of the separatrix with the phase axis are shown as $g_1/(4a)^{1/3}$ and $g_2/(4a)^{1/3}$.

B. Island tune

Let y, p_y be the local coordinates about a fixed point of the Hamiltonian, i.e.,

$$y = \sqrt{2J}\cos\psi - g, \quad p_y = -\sqrt{2J}\sin\psi, \quad (2.19)$$

where g is a fixed point of the Hamiltonian. Making a local coordinate expansion, the Hamiltonian becomes

$$H = \frac{\nu_s a}{4g}\left(1-\frac{g^3}{4a}\right)y^2 + \frac{\nu_s a}{4g}p_y^2 + \cdots. \quad (2.20)$$

Therefore the fixed point g is a stable fixed point if $(1 - g^3/4a) \ge 0$. Because $g_a^3/4a \le 0$ and $0 \le g_b^3/4a \le 1$, g_a and g_b are SFP's. On the other hand, $g_c^3/4a \ge 1$, g_c is the UFP. Since the equilibrium beam distribution, which satisfies the Vlasov equation, is in general a functional of the local Hamiltonian, Eq. (2.20) can also provide information on the local distortion of the bunch profile.

The island tune for the small amplitude oscillations is given by

$$\nu_{\text{island}} = \left|\nu_s\left(1-\frac{g^2}{16}\right)-\nu_m\right|\left(1-\frac{g^3}{4a}\right)^{1/2}. \quad (2.21)$$

The island tune around the inner SFP given by g_b at $\nu_m \ll \nu_c$ is approximately given by $\nu_{\text{island}} \approx |\nu_s(1 - \frac{g^2}{16}) - \nu_m|$. This means that the solution of the equations of motion can be approximated by a linear combination of the homogeneous and inhomogeneous solutions [4]. When the modulation tune ν_m approaches ν_c, with $(1 - g_b^3/4a)^{1/2} \to 0$, the island tune for small amplitude oscillation about the inner SFP approaches 0 and the small amplitude island tune for the outer SFP at $\nu_m = \nu_c$ is $\nu_{\text{island}} = 3|\nu_s(1-\frac{g^2}{16})-\nu_m|$. In this region of the modulation frequency, the linear superposition principle would fail. When the modulation frequency becomes larger than the bifurcation frequency so that $(1-\frac{g^3}{4a})^{1/2} \to 1$, we obtain again $\nu_{\text{island}} = |\nu_s(1 - \frac{g^2}{16}) - \nu_m|$, and the linear superposition principle is again applicable. The island tune for large amplitude motion about a SFP can be obtained by integrating the equation of motion along the corresponding torus of the Hamiltonian in Eq. (2.13).

C. Separatrix of resonant islands

The equation for the separatrix of the Hamiltonian in Eq.(2.15) is given by

$$\frac{H(J,\psi)}{\nu_s} = \frac{1}{2}xg_c^2 - \frac{1}{64}g_c^4 - \frac{1}{2}ag_c, \quad (2.22)$$

which intersects the phase axis at g_1 and g_2 (see Figs. 2 and 3). Using the notation $h_i = g_i/(4a)^{1/3}$, we can express the intercepts of the separatrix as

$$h_1 = -h_c - \frac{2}{\sqrt{h_c}}, \quad h_2 = -h_c + \frac{2}{\sqrt{h_c}}.$$

These intercepts, shown in Figs. 2 and 3, are useful in determining the maximum phase amplitude of synchrotron motion with external phase modulation.

D. The torus that passes through the origin

For a beam with small bunch area, all particles can be approximately described as having initial phase-space coordinates at the origin. The torus which passes through the origin is of interest in many problems related to phase modulation. The torus which passes through the origin, called the torus-O, satisfies the equation $H(J,\psi) = 0$. The intercepts ϕ_0 of the torus-O with the phase axis are then given by

$$\phi_0(\phi_0^3 - 32x\phi_0 + 32a) = 0, \tag{2.23}$$

where $x = 1 - \frac{\nu_m}{\nu_s}$. When $x \geq x_0 = 2^{1/3}x_c$, or $\nu_m \leq \nu_0 = \nu_s(1 - 2^{1/3}x_c)$, there are three solutions to Eq. (2.23) besides the solution $\phi_0 = 0$. This means that there are two nonintersecting tori with the same zero Hamiltonian value. One of the tori is orbiting about the inner SFP, which is the torus-O, and the other one is orbiting about the outer SFP.

At $x = x_0$, two solutions of Eq. (2.23) become degenerate. This means that the torus-O is also the separatrix of islands. When the separatrix passes through the origin, the phase axis intercept of Eq. (2.23) becomes

$$\hat{\phi}_0(x_0) = -2^{5/3}(4a)^{1/3}. \tag{2.24}$$

At a higher modulation frequency with $x < x_o$, there is only one real root to Eq. (2.23) besides $\phi_0 = 0$. The torus-O is orbiting around the outer SFP. The intercept is then given by

$$\hat{\phi}_0(x) = -(16a)^{1/3}\left\{ \left[\left(1 - \frac{x^3}{2x_c^3}\right)^{1/2} - 1\right]^{1/3} - \left[\left(1 - \frac{x^3}{2x_c^3}\right)^{1/2} - 1\right]^{1/3}\right\}. \tag{2.25}$$

III. EXPERIMENTAL PROCEDURE AND DATA ANALYSIS

The experimental procedure at the IUCF Cooler Ring started with a single bunch of about 3×10^8 protons with kinetic energy of 45 MeV. The cycle time was 10 s. The injected beam was electron cooled for about 3 s. The full width at half maximum bunch length was about 5.4 m (or 60 ns) and its revolution period was 969 ns with an rf frequency of 1.031 48 MHz. The low frequency rf system of the IUCF Cooler Ring at $h = 1$ was used in this experiment. A 150-W solid state power amplifier was used to drive the rf cavity to obtain peak gap voltages of up to 500 V, sufficient to capture a beam with a typical momentum spread of $\frac{\Delta p}{p} = \pm 3 \times 10^{-4}$ from the injection cyclotron.

For the longitudinal rf phase shift experiments, the beam was kicked longitudinally by a phase shifter while the data acquisition system was started 2000 turns before the phase kick. The principle of the phase shifter used was reported earlier [4]. The phase lock feedback loop was switched off in our experiment. The response time of the step phase shift was primarily limited by the inertia of the resonant cavity. At 1 MHz, the quality factor Q of the rf cavity was about 40, resulting in a half-power bandwidth of about 25 kHz. The corresponding response time for a step rf phase shift was $\sim$ 40–50 revolutions. In this experiment, the synchrotron oscillation frequency was chosen to be about 540 Hz, or about 1910 revolutions (turns) in the accelerator.

The subsequent beam-centroid displacements were measured with beam position monitors (BPM), which had an rms position resolution of about 0.1 mm. By averaging the position measurement without a phase kick, the stability of the horizontal closed orbit was measured to be less than 0.02 mm. The momentum deviation is related to the off momentum closed orbit $\Delta x_{\rm CO}$ by $\Delta x_{\rm CO} = D_x \frac{\Delta p}{p}$, where the horizontal dispersion function D_x is about 3.9 m at the high dispersion BPM location. The position signals from the BPM was passed through 3-kHz low pass filter before digitization to remove effects due to coherent betatron oscillations and high frequency noise. The BPM sum signal was used to measure the relative phase of the beam. It was passed through a 1.4-MHz low pass filter to eliminate the high harmonics of the bunch and reduce noise before it was compared with an rf signal in a phase detector. Details of our data acquisition system were reported earlier [4, 7]. Two phase detectors were used during this experiment [8], a type II phase detector with a range of $\pm 90°$ and a type III phase detector with a range of $\pm 180°$. The type III phase detector had a phase error of about $\pm 10°$ near 0°, but was adequate for measuring the synchrotron tunes. For more accurate measurements of phase amplitude response, the type II phase detector was used. To extend the range of our beam phase detection, a type IV phase detector with

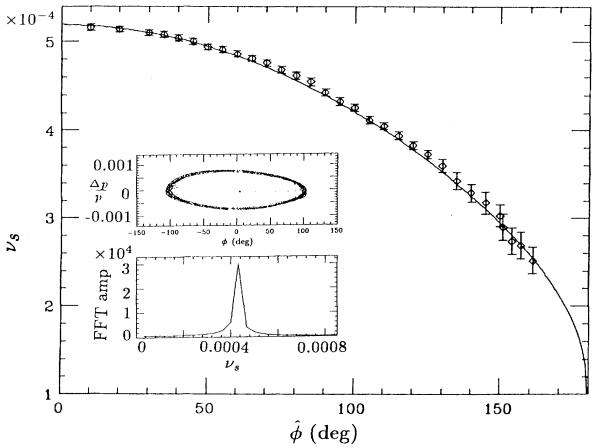

FIG. 4. The dependence of the measured synchrotron tune on the phase amplitude is plotted and compared with theoretical prediction. The Poincaré map in the synchrotron phase space following a phase kick is shown in the top inset. Here, the symbol δ on the ordinate of the inset corresponds to $\frac{\Delta p}{p}$. The scale here is a factor of 2 larger than that of the earlier published data [4], which was in error by a calibration factor of 2.

a range of ±360° has been built for future experiments.

A total of 16 384 points were recorded at ten turn intervals. The top inset in Fig. 4 shows the Poincaré map in the longitudinal phase space, $(\phi, \frac{\Delta p}{p})$. The fast Fourier transform of the phase data is shown in the bottom inset. The resulting synchrotron tune as a function of the peak phase amplitude, shown in Fig. 4, is compared with the theoretical prediction shown as a solid line.

A. Sinusoidal rf phase modulations

When the bunch, initially at $\phi_i = 0$, $\delta_i = 0$, experiences the rf phase sinusoidal modulation with $\varphi = a \sin \nu_m \theta$, where ν_m is the modulation tune and the modulation amplitude $a \ll 1$, the synchrotron phase satisfies the differential equation

$$\ddot{\phi} + \frac{2\alpha}{\omega_0}\dot{\phi} + \nu_s^2 \sin\phi = -a\nu_m^2 \sin\nu_m\theta + \frac{2\alpha}{\omega_0}\nu_m a \cos\nu_m\theta.$$

Here the overdot corresponds to the derivative with respect to the θ variable and ϕ is the particle phase angle relative to the modulated rf phase. Since the measurement time was typically within 150 ms after the phase kick or the start of the rf phase modulation, the effect of electron cooling was not important for these measurements.

The upper left corner of Fig. 5 shows an example of the measured ϕ and $\delta = \frac{h\eta}{\nu_s}\frac{\Delta p}{p}$ vs the turn number at ten turn intervals. The resulting response can be characterized by the response amplitude and the response period. The corresponding Poincaré map is shown in the middle of the figure. Transforming the Poincaré map into the resonant precessing frame discussed in Eqs. (2.10)–(2.13), one obtains an invariant torus-O shown in the lower part of Fig. 5. The winding motion around a smooth torus was oscillating at the frequencies of $2\nu_m$ and $4\nu_m$, which results from the time dependent components of the Hamiltonian in Eq. (2.12). The time dependent winding motion can be suppressed slightly by using the elliptical function data analysis discussed in the Appendix.

It becomes clear that the measured response period corresponds to the period of a torus-O about a SFP and the response amplitude is the intercept of the torus-O with the phase axis. Figure 6 shows the measured response period and response amplitude as a function of the rf modulation frequency along with the prediction of a single particle tracking calculation, which was found to agree well with the experimental data [4]. The response of particle trajectory will trace out a torus-O. At modulation frequencies below a characteristic frequency, i.e., $\nu_m < \nu_0 = (1 - 2^{1/3}x_c)\nu_s$, where x_c is given in Eq. (2.17) and ν_0 is the modulation frequency that the torus-O is also the separatrix (see Sec. II D), the particle trajectory orbits around the inner SFP. At modulation frequencies beyond ν_0, the torus will orbit about the outer SFP. The sharp rise in the observed spectrum at low frequencies and the slowly decrease at high frequencies reflect a characteristic transition of particle trajectories orbiting around different SFP's in the nonlinear parametric

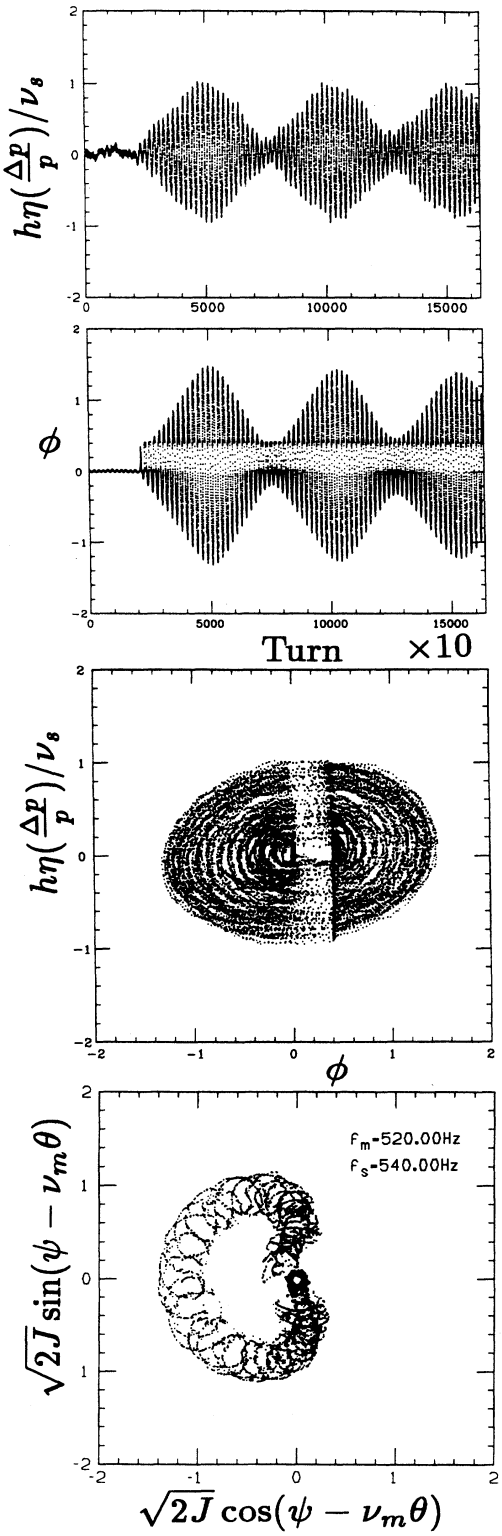

FIG. 5. The normalized off-momentum coordinate δ and the phase ϕ are plotted as a function of revolutions. The data was taken in ten turn intervals. The dead spot of the type III detector is clearly visible. The corresponding Poincaré map is shown in the middle. The Poincaré surface of section (torus-O) in the resonant precessing frame is shown on the lower part of the figure.

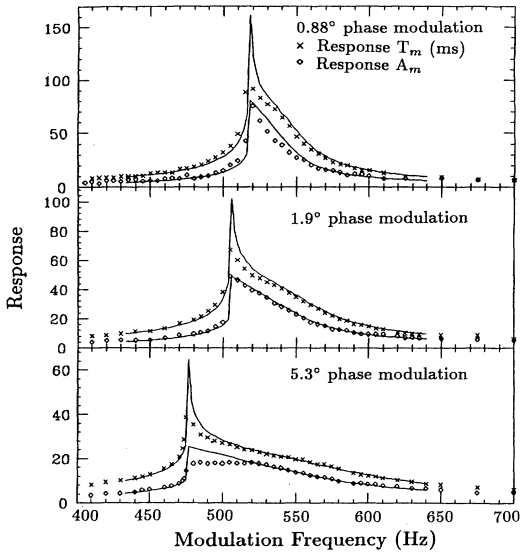

FIG. 6. The measured peak response amplitude and response period are plotted as a function of the driving frequency. Single particle tracking calculations are shown for comparison.

resonant system.

The maximum amplitude response corresponds to the rf modulation frequency where the torus-O is also the separatrix, which occurs at $x = x_0$, i.e., the frequency that $g_2 = 0$ in Fig. 3. Thus the peak responses of both the amplitude and the period will occur at the same modulation frequency (see Sec. II D) given by

$$\nu_{m,p} = \nu_s[1 - \tfrac{3}{8}(2a)^{2/3}], \tag{3.1}$$

with the peak phase amplitude $|\hat{\phi}| = 2^{5/3}(4a)^{1/3}$ given by Eq. (2.24). The peak response period is infinite when the torus-O is also the separatrix. This feature is visible from the single particle tracking calculation shown as solid lines in Fig. 6.

It is worth pointing out that the above analytic solution is derived from the perturbative expansion in terms of the action-angle variable which is limited to $J \leq 2$. Therefore when the phase modulation amplitude is larger than 5°, particle motion cannot be described by the method discussed in Sec. II at the modulation frequency around $\nu_{m,p}$ of Eq. (3.1) because the maximum amplitude will exceed this limit. At higher modulation amplitudes, our numerical simulations show that particles can jump outside the rf bucket (the stable region in the longitudinal phase space) and then be recaptured in the same bucket ($h = 1$ rf system). When the bunch is moving outside the rf bucket, beam decoherence also occurs. Some of our data exhibited this decoherence at large modulation amplitudes.

B. Invariant tori derived from experimental data

In one case, the beam was kicked with a phase shifter of about 42° and the rf system was then modulated with sinusiodal phase modulation with phase amplitude $a = 1.45°$. Figure 7 shows the measured Poincaré map of the normalized longitudinal phase space at the top and the corresponding Poincaré surface of section in the resonant frame at the bottom. Note that the phase kick took about 40–50 revolutions to reach its intended phase kicked amplitude visible from Fig. 7. In this run, we used the type II phase detector, which did not have the dead area around 0°. However, this phase detector was limited at ±90°. The trajectory of beam bunch in the presence of external rf phase modulation traced out a torus determined by the initial phase-space coordinates of the bunch. Since the torus, which passed through a fixed set of initial phase-space coordinates, depended on the rf phase modulation frequency, the measured tori would depend on the driven frequency. Figure 8 displays a sample of invariant tori deduced from the experimental data. The solid lines are invariant tori of the Hamiltonian in Eq. (2.13), where the synchrotron frequency was fitted to be about 535±3 Hz.

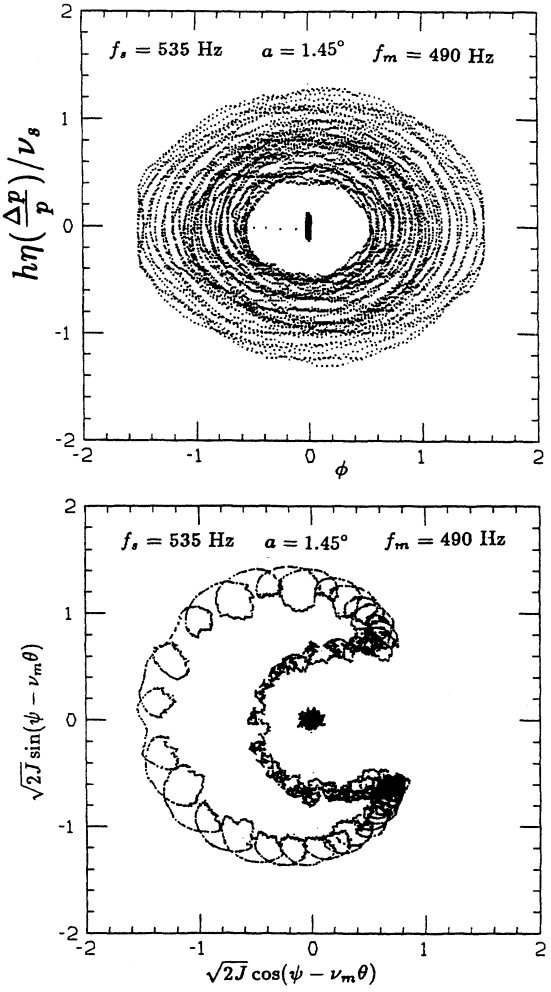

FIG. 7. The Poincaré map for the bunch experiencing sinusoidal rf phase modulation with amplitude 1.45° after an initial phase kick of 42° is shown for $f_m = 490$ Hz in the upper part of the figure. The corresponding Poincaré surface of section in the resonant frame is shown in the lower part of the figure for comparison.

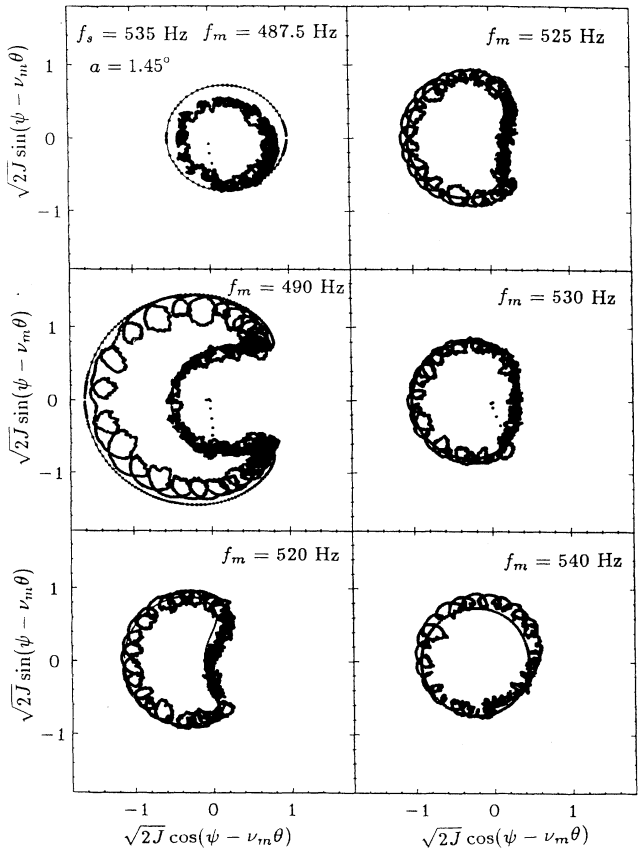

FIG. 8. The Poincaré surface of section at the resonant frame for different modulation frequencies at a fixed initial phase kick amplitude is shown in comparison with theoretical prediction of the time independent Hamiltonian Eq. (2.13).

C. Experimental observation at the third synchrotron harmonic

From the result of Sec. II, we notice that the phase modulation at even multiples of synchrotron frequency does not give rise to coherent parametric resonances. Our experiemntal results verified indeed that there was no apparant response at the second harmonic of the synchrotron frequency. However, the theory indicates that when the modulation frequency is equal to odd multiples of the synchrotron frequency, the parametric resonance becomes important. We have performed experimental measurements for $\nu_m \approx 3\nu_s$.

Instead of measuring the transient solutions by using our data acquisition system, we measured the steady-state solution in this later experiment. The beam was injected and modulated by the rf phase shifter in an 11-s cycle time. The measurement was performed 7 s after injection. We chose the synchrotron frequency to be about 261 Hz with an rf phase modulation amplitude a of 6°. The longitudinal beam distribution obtained from the signal of the BPM sum signal displayed on the oscilloscope triggered at the rf frequency is shown in Fig. 9. Since the damping exponential-folding time was about 0.34 s, sufficient time was allowed for particles to damp into parametric resonant islands of the Hamiltonian. Therefore, the beam was observed to split into beamlets as shown in Fig. 9. The outer beamlets will circulate about the center of the phase space at the frequency of $\nu_m/3$, which is the synchrotron frequency at the island amplitude. Detailed information about these attractors (islands) could be obtained by kicking a tightly bunched beamlet into these resonance islands for Poincaré map tracking. Such a process becomes difficult when the stable region of the attractor is small. In such a situation, there is little information that can be gained from the digitized phase information of our phase detector. We measured instead the phase amplitude of attractors from the oscilloscope trace of a BPM sum signal, the results of which are tabulated in Table I.

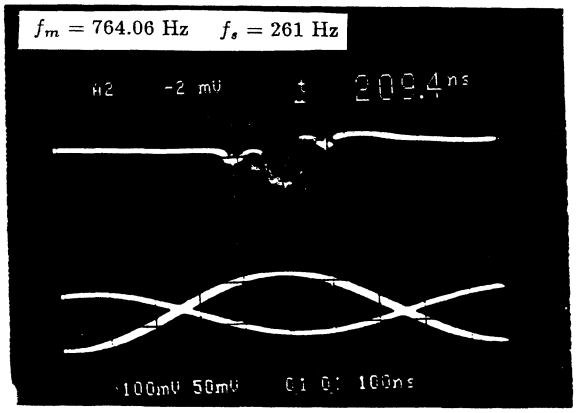

FIG. 9. The effect of the rf phase modulation at the third harmonic of the synchrotron frequency. Note here that the synchrotron phase space in the resonant frame has three SFP's and three UFP's besides the SFP at the origin.

The resonant Hamiltonian at the third synchrotron harmonic is given by [10]

$$H = \left(\nu_s - \frac{\nu_m}{3}\right) J - \frac{\nu_s J^2}{16} - \frac{\nu_s a (2J)^{3/2}}{48} \cos 3\psi, \qquad (3.2)$$

which has seven fixed points of which four are stable and three are unstable. The phase amplitudes of these fixed points are

$$g_{\mathrm{SFP}} = \frac{a + \sqrt{a^2 + 64(1 - \frac{\nu_m}{3\nu_s})}}{2},$$
$$g_{\mathrm{UFP}} = \frac{\sqrt{a^2 + 64(1 - \frac{\nu_m}{3\nu_s})} - a}{2}. \qquad (3.3)$$

TABLE I. The phase amplitude of outer beamlet measured from the oscilloscope.

	f_s (Hz)	260	261	262
f_m (Hz)	$\hat{\phi}$ (deg) (data)		g_{SFP} (deg) [Eq.(3.3)]	
763.08	41.0 ± 2.0	36.9	39.7	42.3
764.06	39.0 ± 2.0	35.9	38.8	41.4

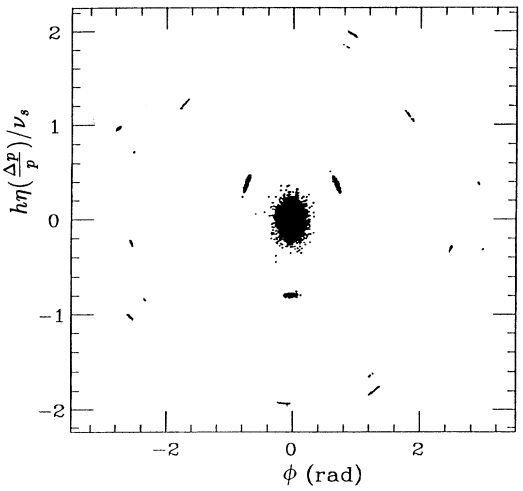

FIG. 10. The final beam profile distribution at about 5×10^5 revolutions obtained from a numerical simulation of the synchrotron motion starting from a uniform phase-space distribution of $\phi_i \in [-\pi, \pi]$ and $\delta_i \in [-2, 2]$ with rf phase-modulation frequency $f_m = 2.88 f_s$, the modulation amplitude $a = 6°$, and the damping parameter $\alpha = 2.5\ \mathrm{s}^{-1}$.

Table I compares the measured phase amplitude in the second column with the SFP calculated from Eq. (3.3) at synchrotron frequencies 260, 261, and 262 Hz, where $f_s = 261$ Hz fits better the island amplitude. The "steady-state" beam distribution after about 5×10^5 revolutions obtained from the numerical simulations with an initially uniform particle distribution in the phase space is shown in Fig. 10. Tracking results confirm that SFP's of the third harmonic modulation become attractors in the weak dissipative system. Besides the three dominant resonant islands, the tracking results show that there are many more islands beyond the validity of our perturbative treatment discussed in Sec. II. Since those islands with large phase amplitudes are small, it will be difficult to observe them experimentally.

IV. CONCLUSION

An experimental study of the rf phase modulation has been carried out. When the phase-space motion is transformed into the resonant rotating frame, the invariant tori around fixed points of the Hamiltonian plays an essential role in describing the dynamics of driven synchrotron motion. The complicated phase-space motion is replaced by a simple predictable invariant of the Hamiltonian flow. The observed response amplitude and period can then be calculated analytically based on the time independent Hamiltonian. The remaining time dependent components of the Hamiltonian are found to create small winding motion around an invariant torus dominantly at the frequency $2\nu_m$. The orbit perturbation arises mainly from the coherent perturbation of the parametric resonance. We also observed that there was no apparent response to the rf phase modulation at the second harmonic of the synchrotron frequency. At the third synchrotron harmonic, the measured phase amplitude of attractors agreed with the stable fixed points of the resonance Hamiltonian. Better understanding of synchrotron motion in circular accelerators will benefit the design and operation of future storage rings and colliders. These studies may also be useful in evaluating the feasibility of using the rf noise for a superslow extraction in high-energy colliders.

ACKNOWLEDGMENTS

This work was supported in part by the National Science Foundation, Grant No. NSF PHY-9221402, and by the U.S. Department of Energy, Grant No. DE-FG02-93ER40801.

APPENDIX: THE ACTION ANGLE OF THE UNPERTURBED HAMILTONIAN

Let the Hamiltonian of Eq. (2.3) be divided into the unperturbed Hamiltonian H_0 and the perturbation Hamiltonian H_1,

$$H_0 = \frac{1}{2}\nu_s \delta^2 + 2\nu_s \sin^2 \frac{\phi}{2}, \tag{A1}$$

$$H_1 = \nu_m a \delta \cos \nu_m \theta. \tag{A2}$$

Here the unperturbed synchrotron phase-space coordinates are relative to the fixed revolution frequency reference frame. However, the phase-space coordinates (ϕ, δ) in Eq. (2.3) are referenced to the rf phase modulated coordinate system. When the amplitude of the rf phase modulation is small, the reference frame with respect to the revolution frequency and the reference frame with respect to the rf wave are nearly identical, and the method described here offers the advantage of extending the range of validity of the action-angle expansion.

Expressing the synchrotron coordinates in terms of the parameters (k, w)

$$\sin \frac{\phi}{2} = k \sin w, \quad \frac{\delta}{2} = k \cos w, \tag{A3}$$

one obtains $H_0 = 2\nu_s k^2$. Thus the action of the unperturbed Hamiltonian becomes

$$J = \frac{1}{2\pi} \oint \delta d\phi = \frac{8}{\pi}[E(k) - (1 - k^2)K(k)], \tag{A4}$$

where the complete elliptical functions are given by [9]

$$E(k) = \int_0^{\frac{\pi}{2}} \sqrt{1 - k^2 \sin^2 w}\ dw,$$

$$K(k) = \int_0^{\frac{\pi}{2}} \frac{1}{\sqrt{1 - k^2 \sin^2 w}}\ dw\ .$$

The *synchrotron tune* is obtained from the Hamilton's equation of motion, i.e.,

$$\dot{\psi} = \frac{\partial H_0}{\partial J} = \nu_s \frac{\pi}{2K}, \tag{A5}$$

where we have used the identities

$$2k^2\frac{dE(k)}{dk^2} = E(k) - K(k),$$
$$2k^2\frac{dK(k)}{dk^2} = \frac{1}{1-k^2}E(k) - K(k).$$

The angle variable ψ, which is conjugate to the action J, can be obtained by integrating Eq. (A5),

$$\psi = \frac{\pi\nu_s}{2K}\theta + \psi_0.$$

The task is to express the normalized off-momentum coordinate δ in the perturbed Hamiltonian H_1, in Fourier harmonics of the conjugate angle ψ. Using Hamilton's equation $\dot{\phi} = \nu_s\delta$, we can relate the orbital angle θ to the w parameter of Eq. (A3) as

$$\nu_s(\theta - \theta_0) = \int_{\phi_0}^{\phi}\frac{d\phi}{\delta} = u - u_0,$$

where

$$u = \int_0^w \frac{1}{\sqrt{1-k^2\sin^2 w}}dw,$$
$$u_0 = \int_0^{w_0} \frac{1}{\sqrt{1-k^2\sin^2 w}}dw.$$

Here the Jacobian elliptical function is then defined as

$$\sin w = \mathrm{sn}(u|k), \quad \cos w = \mathrm{cn}(u|k).$$

Thus the expansion of the δ in Fourier harmonics of ψ is equivalent to the expansion of $\mathrm{cn}(u|k)$ in $\psi = \frac{\pi u}{2K}$. The task can be achieved by using the formula of Eq. (16.23.2) in Ref. [9], i.e.,

$$\mathrm{cn}(u|k) = \frac{2\pi}{kK(k)}\sum_0^\infty \frac{q^{n+1/2}}{1+q^{2n+1}}\cos(2n+1)\psi, \tag{A6}$$

where ψ is the synchrotron phase with the q parameter given by

$$q = e^{-\pi K'/K} = \frac{k^2}{16} + 8\left(\frac{k^2}{16}\right)^2 + 84\left(\frac{k^2}{16}\right)^3 + 992\left(\frac{k^2}{16}\right)^4 + \cdots,$$

with $K'(k) = K(\sqrt{1-k^2})$. For synchrotron motion with small action $J \le 2$, we use the power series expansion, i.e.,

$$K(k) = \frac{\pi}{2}\left[1 + \left(\frac{1}{2}\right)^2 k^2 + \left(\frac{1\times 3}{2\times 4}\right)^2 k^4 + \left(\frac{1\times 3\times 5}{2\times 4\times 6}\right)^2 k^6 + \cdots\right],$$

$$E(k) = \frac{\pi}{2}\left[1 - \left(\frac{1}{2}\right)^2\frac{k^2}{1} - \left(\frac{1\times 3\times 5}{2\times 4\times 6}\right)^2\frac{k^6}{5} - \cdots\right],$$

to obtain

$$J = 2k^2\left(1 + \frac{1}{8}k^2 + \frac{3}{64}k^4 + \cdots\right), \tag{A7}$$

$$k^2 = \frac{J}{2}\left(1 - \frac{1}{16}J - \frac{1}{256}J^2 - \cdots\right). \tag{A8}$$

Thus the off-momentum variable δ can be expressed as

$$2k\mathrm{cn}(u|k) = (2J)^{1/2}\cos\psi + \frac{(2J)^{3/2}}{64}\cos 3\psi + \frac{(2J)^{5/2}}{4096}\cos 5\psi + \cdots. \tag{A9}$$

Substituting the expansion of the elliptical cosine function into Eq. (A2), one obtains the Hamiltonian in terms of action-angle variable similar to that of Eq. (2.8). The leading order terms in these two expansions are identical. They begin to deviate from each other at the higher order harmonics. The difference is small.

Using the elliptical functions for our data analysis, we can calculate the k value from the measured phase-space coordinates (ϕ, δ) by using the relation of Eq. (A3),

$$k^2 = \frac{\delta^2}{4} + \sin^2\frac{\phi}{2}. \tag{A10}$$

The action can be obtained from Eq. (A4) or Eq. (A7). The synchrotron phase ψ can be obtained from the expansion

$$\frac{\delta}{2\sin\frac{\phi}{2}} = \frac{\pi}{2K}\tan\left(\frac{\pi}{2} - \psi\right) - \frac{2\pi}{K}\sum_{n=1}^{\infty}\frac{q^{2n}}{1+q^{2n}}\sin 2n\psi. \tag{A11}$$

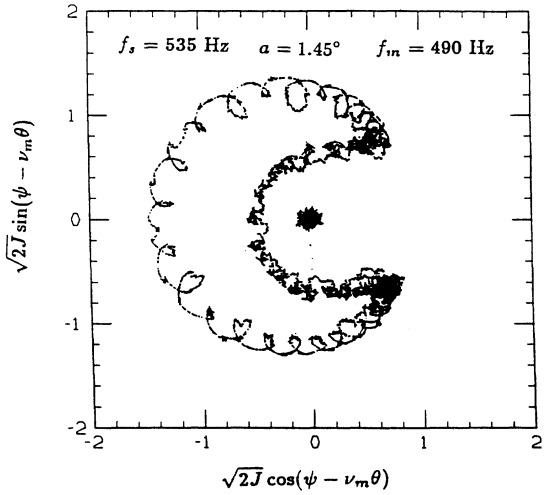

FIG. 11. The Poincaré map in the resonant precessing frame obtained by using the elliptical function data analysis is shown for an rf phase-modulation amplitude 1.45° at f_m = 490 Hz following a 42° initial phase kick. The result should be compared with that of Fig. 7 obtained from the Bessel function data analysis of Sec. II.

For synchrotron motion with a relatively large k, a better approximation for the data analysis can be obtained using the polynomial approximation of Eqs. (17.3.34) and (17.3.36) of Ref. [9] to evaluate $K(k), E(k)$, and q functions in order to obtain the action angle J and ψ. For each data point (ϕ, δ), Eq. (A10) is used to calculate k. The action J is then obtained from Eq. (A4). The corresponding angle variable ψ is obtained from Eq. (A11). The Poincaré map in the resonant frame is then given by phase-space points in $(\sqrt{2J}\cos(\psi - \nu_m\theta), \sqrt{2J}\sin(\psi - \nu_m\theta))$ shown in Fig. 11 for the same data set as that of Fig. 7. We found that the winding motion in the Poincaré map observed in Fig. 7 became less pronounced for large amplitude oscillations shown in Fig. 11. This indicates that the time independent Hamiltonian is suppressed in the data analysis by using the elliptical functions. The characteristic feature remains identical to the simpler approach discussed in Sec. II.

[1] D. Boussard, *et al.*, IEEE Trans. Nucl. Sci. **NS-26**, 3484 (1979); in *Proceedings of the 11th International Conference on High Energy Accelerators*, edited by W.S. Newman (Birkhauser, Basel, 1980), p. 620; G. Dôme, CERN Advanced Particle Accelerator School, CERN Report No. 87-03, p. 370, 1987 (unpublished); S. Krinsky and J.M. Wang, Part. Accel. **12**, 107 (1982); J.A. Ellison, B.S. Newberger, and H.J. Shih, in *Proceedings of the 1991 IEEE Particle Accelerator Conference,* edited by L. Lizama and J. Chew (IEEE, New York, 1991), p. 216; H.J. Shih, J. Ellison, B. Newberger, and R. Cogburn, SSCL Report No. SSCL-578, 1992 (unpublished); W. Gabella *et al.*, Fermilab Report No. TM-1783, 1992 (unpublished).

[2] E.D. Courant and H.S. Snyder, Ann. Phys. (N.Y.) **3**, 1 (1958).

[3] M. Syphers *et al.*, Phys. Rev. Lett. **71** 719 (1993); Y. Wang *et al.* (unpublished).

[4] M. Ellison *et al.*, Phys. Rev. Lett. **70**, 591 (1993).

[5] E.M. McMillan, Phys. Rev. **68**, 143 (1945); V.I. Veksler, C. R. Acad. Sci. U.S.S.R. **43**, 329 (1944); **44**, 365 (1944).

[6] L.D. Landau and E.. Lifschitz, *Mechanics*, 3rd ed. (Pergamon Press, Oxford, 1976); D. D'Humieres, M.R. Beasley, B.A. Huberman, and Libchaber, Phys. Rev. A **26**, 3483 (1982); T. Ieiri and K. Hirata, *Proceedings of the IEEE Particle Accelerator Conference Chicago, 1989* (IEEE, New York, 1989), p. 926; M. Octavio, Phys. Rev. B **29**, 1231 (1984); S.W. McDonald *et al.*, Physica D **17**, 125 (1985).

[7] S.Y. Lee *et al.*, Phys. Rev. Lett. **67**, 3768 (1991); D.D. Caussyn *et al.*, Phys. Rev. A **46**, 7942 (1992).

[8] Roland E. Best, *Phase Locked Loops, Theory, Design, and Applications* (McGraw-Hill, New York, 1984), pp. 7–9. The type II phase detector utilizes the XOR logic, and the type III phase detector utilizes the edge-triggered JK-master-slave flip-flop circuit.

[9] *Handbook of Mathmatical Functions,* Nat. Bur. Stand. Appl. Math. Ser. No. 55, edited by M. Abramowitz and I.A. Stegun (U.S. GPO, Washington, DC, 1970).

[10] Using the elliptical function data analysis discussed in the Appendix, the strength of the third order driving amplitude $a/48$ of Eq. (3.2) should be replaced by $a/64$, shown in Eq. (A9). The phase amplitude of SFP and UFP of Eq. (III C) is then modified by replacing a with $3a/4$. This implies that the phase amplitudes of SFP and UFP depend weakly on the modulation amplitude.